LETTER

https://doi.org/10.1038/s41586-018-0803-x

The corona contracts in a black-hole transient

E. Kara[1,2,3,4]*, J. F. Steiner[4], A. C. Fabian[5], E. M. Cackett[6], P. Uttley[7], R. A. Remillard[4], K. C. Gendreau[2], Z. Arzoumanian[2], D. Altamirano[8], S. Eikenberry[9,10], T. Enoto[11], J. Homan[12,13], J. Neilsen[14] & A. L. Stevens[15]

The geometry of the accretion flow around stellar-mass black holes can change on timescales of days to months[1–3]. When a black hole emerges from quiescence (that is, it 'turns on' after accreting material from its companion) it has a very hard (high-energy) X-ray spectrum produced by a hot corona[4,5] positioned above its accretion disk, and then transitions to a soft (lower-energy) spectrum dominated by emission from the geometrically thin accretion disk, which extends to the innermost stable circular orbit[6,7]. Much debate persists over how this transition occurs and whether it is driven largely by a reduction in the truncation radius of the disk[8,9] or by a reduction in the spatial extent of the corona[10,11]. Observations of X-ray reverberation lags in supermassive black-hole systems[12,13] suggest that the corona is compact and that the disk extends nearly to the central black hole[14,15]. Observations of stellar-mass black holes, however, reveal equivalent (mass-scaled) reverberation lags that are much larger[16], leading to the suggestion that the accretion disk in the hard-X-ray state of stellar-mass black holes is truncated at a few hundreds of gravitational radii from the black hole[17,18]. Here we report X-ray observations of the black-hole transient MAXI J1820+070[19,20]. We find that the reverberation time lags between the continuum-emitting corona and the irradiated accretion disk are 6 to 20 times shorter than previously seen. The timescale of the reverberation lags shortens by an order of magnitude over a period of weeks, whereas the shape of the broadened iron K emission line remains remarkably constant. This suggests a reduction in the spatial extent of the corona, rather than a change in the inner edge of the accretion disk.

MAXI J1820+070[19] (ASASSN-18ey[21]) was discovered on 2018 March 11 with the Monitor of All-sky X-ray Image (MAXI) on board the International Space Station (ISS). The next day, the Neutron star Interior Composition Explorer (NICER)[22], also an ISS payload, started obtaining detailed observations and has continued observing since, at a cadence of 1–3 days[20]. The NICER X-ray Timing Instrument consists of an aligned collection of 52 active paired X-ray 'concentrator' optics and silicon drift detectors, which record the arrival times and energies of individual X-ray photons. It provides a timing resolution of less than 100 ns (25 times faster than NASA's previous best X-ray timing instrument, the Rossi X-ray Timing Explorer) and the highest-ever soft band peak effective area of 1,900 cm^2 (nearly twice that of the timing-capable EPIC-pn camera on the space observatory X-ray Multi-Mirror Mission (XMM-Newton), all while providing good spectral resolution (145 eV at 6 keV), minimal pile-up on bright sources and very little dead time. MAXI J1820+070 regularly reached 25,000 counts per second in NICER's 0.2–12-keV band, while still providing high-fidelity spectral and timing products (for comparison, the XMM-Newton detectors become piled up at rates of 600–800 counts per second[23]). This high count rate allows us to probe timescales that are nearly an order of magnitude shorter than is possible using XMM-Newton. Owing to the enormous size of the dataset, in this Letter, we describe only the spectral-timing results of a subset of the total NICER observations (Extended Data Table 1 and Fig. 1a, b) when the source was brightest (luminosity $L_{0.3-10\,\mathrm{keV}}/L_{\mathrm{Edd}} = 0.04–0.06$, where L_{Edd} is the Eddington luminosity, and using the parallax distance measure[24,25] of about 3.3 kpc and assuming a $10M_{\odot}$ black hole, where $M_{\odot}$ is the solar mass). More detail on the remaining observations can be found in Methods.

Figure 1c shows a simple ratio of the spectra from the six epochs we study here to a power-law model fit to the 3–10-keV band. The photon index and normalization are left free to vary between observations (see Methods for a description of the data reduction). All six epochs show a remarkably constant broad iron (Fe) K emission line that extends down below 5 keV. This is best fitted by relativistic reflection from a point-source X-ray corona at a height of less than $5r_{\mathrm{g}}$, where the gravitational radius $r_{\mathrm{g}} = GM/c^2$, irradiating a disk with an inner radius of less than $2r_{\mathrm{g}}$. In addition, there is a narrow feature at 6.4 keV that is clearly present at early times (with an equivalent width of about 50 eV), but is less prominent in later epochs (down to an equivalent width of about 10 eV). The spectral modelling of MAXI J1820+070 will be presented in detail shortly (A.C.F. et al., manuscript in preparation).

To explore the time-dependence of these spectral signatures, we performed a frequency-resolved timing analysis (see Methods for details and Extended Data Fig. 1 for the 0.01–100-Hz power spectrum of each epoch). We examined the frequency-dependent time lag between the 0.5–1-keV and 1–10-keV emission for the six epochs (Fig. 2). At low Fourier frequencies (at a few hertz and below), we observed a positive lag, defined as the hard band following after the soft band, at all epochs (see Methods; Extended Data Fig. 2). The low-frequency hard lag is a nearly ubiquitous feature of Galactic black-hole binaries in the hard and intermediate states[26,27] and also of type 1 active galactic nuclei (AGN)[28]. The low-frequency hard lags are usually interpreted as due to fluctuations in the mass accretion rate in the disk that propagate inwards on a viscous timescale, causing soft photons to respond before hard photons do[29].

At high frequencies, the lags show a reversal of sign, where the soft band begins to lag behind the hard. The soft lag is found in all observations at 4.5σ confidence or greater (see Methods for details). This suppression of the hard continuum lag is often seen in AGN systems, but is rarely seen in Galactic black-hole binaries, where usually the hard lag continues to dominate over all variability timescales that can be probed. High-frequency soft lags are usually interpreted as due to reflection off the inner accretion flow. In Galactic black-hole binaries, the hard X-ray corona irradiates the accretion disk, reheating the disk and causing a lag of the thermal emission on the shortest timescales[16]. In these epochs (and confirmed in the other NICER observations; Extended Data Fig. 4a), we observed a trend of the soft lag towards progressively shorter timescales, suggesting an evolution in the accretion flow itself. This evolution towards a smaller emitting region has

[1]University of Maryland, College Park, MD, USA. [2]NASA Goddard Space Flight Center, Greenbelt, MD, USA. [3]Joint Space Science Institute, University of Maryland, College Park, MD, USA. [4]MIT Kavli Institute for Astrophysics and Space Research, Cambridge, MA, USA. [5]Institute of Astronomy, Cambridge, UK. [6]Wayne State University, Department of Physics and Astronomy, Detroit, MI, USA. [7]Anton Pannekoek Institute for Astronomy, University of Amsterdam, Amsterdam, The Netherlands. [8]School of Physics and Astronomy, University of Southampton, Southampton, UK. [9]Department of Astronomy, University of Florida, Gainesville, FL, USA. [10]Department of Physics, University of Florida, Gainesville, FL, USA. [11]Hakubi Center for Advanced Research and Department of Astronomy, Kyoto University, Kyoto, Japan. [12]Eureka Scientific, Oakland, CA, USA. [13]SRON, Netherlands Institute for Space Research, Utrecht, The Netherlands. [14]Villanova University, Department of Physics, Villanova, PA, USA. [15]Department of Physics and Astronomy, Michigan State University, East Lansing, MI, USA. *e-mail: ekara@astro.umd.edu

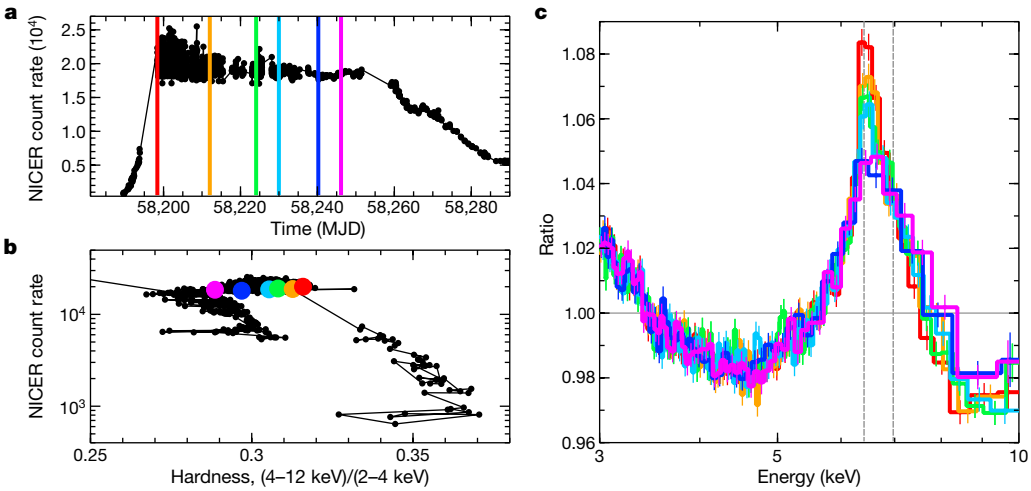

Fig. 1 | Overview of MAXI J1820+070 in the hard state. a, The long-term 0.2–12-keV NICER light curve of MAXI J1820+070 in the hard state (black) overplotted with the times of the six NICER observations that are the subject of this analysis. After MJD 58,290, the source began to transition rapidly to the soft state; Extended Data Fig. 4b. **b**, The NICER hardness–intensity diagram, defined as the total 0.2–12-keV count rate (in units of counts per second) versus the ratio of hard (4–12 keV) to soft (2–4 keV) count rates. The black points show MAXI J1820+070 from its time of discovery to 2018 June 20. The six epochs of interest are shown as the coloured points. We focus on a luminous phase, during which the source gradually became softer with time, but remained always in the hard, corona-dominated state. Error bars (1σ) are similar to the size of the points. **c**, The corresponding spectra of the six epochs fitted to a simple power law in the 3–10-keV range (with normalization and photon index free to vary between observations). The ratio of the 3–10-keV spectrum to the best-fitting power-law plot reveals a clear broad Fe K emission line, and a narrow component at 6.4 keV that decreases in equivalent width as the source evolves in time. Thin grey vertical lines indicate Fe Kα at 6.4 keV and H-like Fe XXVI at 6.97 keV. Error bars indicate 1σ confidence intervals.

been inferred both spectroscopically[8,11], and separately through timing properties[9,17], but the absolute size scale of the emitter remains unclear, and also whether it is the corona that is becoming more compact or the truncation radius of the disk that is decreasing. The evolution of the thermal reverberation lags to higher frequencies, together with the unchanging shape of the Fe line profile, suggest that the evolution is driven by the corona.

To examine the high-frequency lags further, we measured the inter-band time delays by averaging over the frequencies where the soft lag is detected in Fig. 2 (although extending to a slightly broader frequency range for late-time epochs to maximize the signal-to-noise ratio). The lag is measured between each small energy bin and a broad reference band, taken to be from 0.5 keV to 10 keV (with the bin of interest removed so that the noise is not correlated).

Figure 3 shows the high-frequency lag–energy spectra for each of the six epochs. We see a thermal lag below 1 keV, and additionally, at higher energies, the lag peaks around the Fe K emission line at about 6.4 keV, reminiscent of the Fe K reverberation lags commonly observed in AGN systems. These Fe K lags are not all statistically significant compared to a featureless power-law lag (see Methods and Extended Data Fig. 3) and are not present in all observations (Extended Data Fig. 4), but if associated with Fe K reverberation, we found an average amplitude of time delay 0.47 ± 0.08 ms or $(14 \pm 3)r_g/c$ for an assumed black-hole mass of $10M_\odot$ (see Methods for a description of how the amplitude is estimated and how this translates to a light travel-time delay by accounting for dilution and lags due to propagating fluctuations). The thermal reverberation lag persisted at high frequencies (about 10−100 Hz) until the source transitioned to the soft state and the root-mean-square variability of the source decreased (Extended Data Fig. 4).

Previous results on the hard state of GX 339-4 observed with XMM-Newton revealed thermal lags[16,17], and a tentative Fe K lag[18], that are more than an order of magnitude larger than the reverberation lags reported here. This has been interpreted as a large truncation radius of the disk of about $100r_g$, which is at odds with other estimates of the inner radius from spectral fitting of the gravitationally redshifted broad Fe line that suggest a truncation radius of about $2r_g$ and a coronal height[11,30] of about $10r_g$. NICER, with its large effective area, minimal pile-up and good spectral resolution, has revealed a consistent picture of spectral and time lag results for MAXI J1820+070, which point to a compact corona and small truncation radius. At frequencies of less than a few hertz, the time lags in MAXI J1820+070 are very similar in shape and amplitude to those of GX 339-4, and so we suggest it is possible that similarly short-timescale Fe K reverberation would be seen in GX 339-4, if we could probe high enough frequencies to overcome the dominating continuum lag.

The simultaneous detection of an unchanging broad Fe line component (Fig. 1c) together with short reverberation lags that evolve to higher frequencies (Figs. 2, 3) suggest that the X-ray-emitting region is

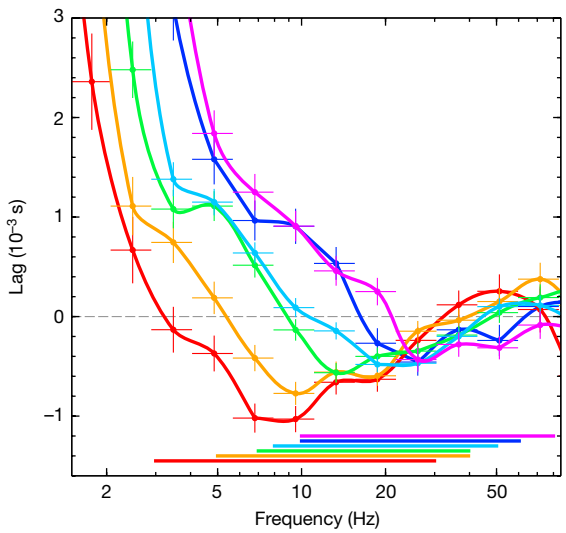

Fig. 2 | The evolution of the lag–frequency spectra. The evolution of the lag between 0.5–1 keV and 1–10 keV is shown as a function of temporal frequency for our six observation epochs. Colour-coding is as in Fig. 1. The points are connected with a Bezier join to guide the eye. A negative lag indicates that the soft band follows behind the hard band. The soft lag evolves to higher frequencies with time. The solid lines on the bottom portion of the figure indicate the frequencies used in the lag–energy analysis (Fig. 3). Vertical error bars indicate 1σ confidence intervals and horizontal error bars indicate the frequency binning.

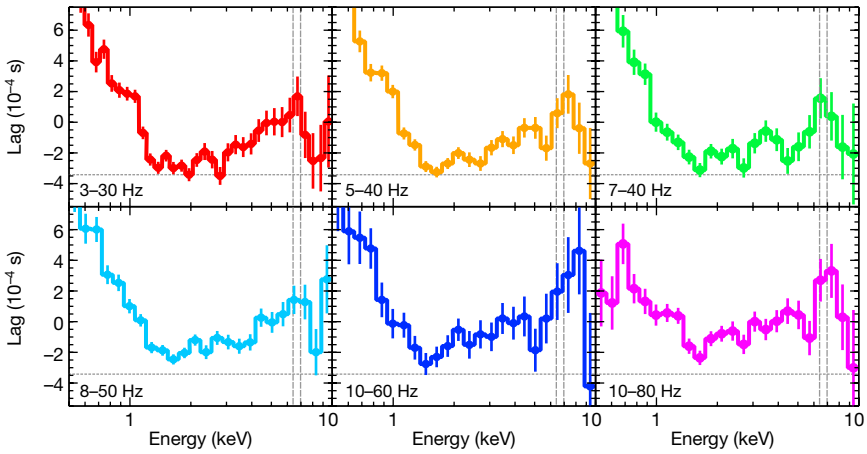

Fig. 3 | The high-frequency lag–energy spectra. Shown is the evolution of the lag–energy spectra for the six observation epochs. The Fourier frequency at which the thermal lag is found increases with time (as is also evident in Fig. 2). There are hints of an Fe K lag in these six epochs. Thin grey vertical lines indicate Fe Kα at 6.4 keV and H-like Fe XXVI at 6.97 keV. The horizontal line indicates the minimum lag of the first epoch, as a reference by which to compare to subsequent epochs. Error bars indicate 1σ confidence intervals.

spatially compact, and becoming more compact over time. This could be accomplished by a vertically extended corona with a compact core, which collapses down along the axis over time (see schematic in Fig. 4). The 3–10-keV spectra suggest a similar evolution, where, in addition to the unchanging relativistically broadened Fe line, there is a second, narrow, 6.4-keV component that is only prominent at early times. If this narrow component is due to a vertically extended corona irradiating large radii, then, as the corona collapses, the solid angle irradiating the disk at large radii decreases, thus decreasing the equivalent width of the narrow component. The fact that the thermal reverberation lags remain throughout all epochs and that the spectral shape of the broad Fe line component is constant over time suggests that there is little or no evolution in the truncation radius of the inner disk during the luminous hard state. These observations of a Galactic black hole in its hard state are similar to observations of local Seyfert galaxies, which show a compact X-ray corona and a disk that extends to very small radii. NICER continues to take almost-daily observations of MAXI J1820+070 and other Galactic black-hole transients, thus providing a new tool for understanding accretion physics near the black-hole event horizon.

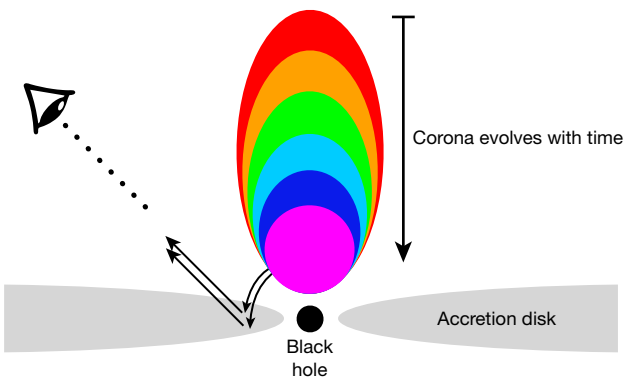

Fig. 4 | Schematic of the proposed geometry. Shown is a schematic of the proposed geometry, evolving from a vertically extended corona at early times to a more compact corona at late times. The corona has a static core at small radii that is responsible for most of the flux irradiating the disk, and the constant shape of the broad Fe line is due to this static core. As the corona decreases in vertical extent, the coronal variability timescale shortens, causing the shift in the thermal reverberation lag to higher frequencies. The decrease in vertical extent of the corona is also responsible for the decrease in the equivalent width of the narrow component of the Fe line at 6.4 keV.

Online content

Any methods, additional references, Nature Research reporting summaries, source data, statements of data availability and associated accession codes are available at https://doi.org/10.1038/s41586-018-0803-x.

Received: 9 July 2018; Accepted: 17 October 2018;
Published online 9 January 2019.

1. Remillard, R. A. & McClintock, J. E. X-ray properties of black-hole binaries. *Annu. Rev. Astron. Astrophys.* **44**, 49–92 (2006).
2. Fender, R. P., Belloni, T. M. & Gallo, E. Towards a unified model for black hole X-ray binary jets. *Mon. Not. R. Astron. Soc.* **355**, 1105–1118 (2004).
3. Done, C., Gierliński, M. & Kubota, A. Modelling the behaviour of accretion flows in X-ray binaries. Everything you always wanted to know about accretion but were afraid to ask. *Astron. Astrophys. Rev.* **15**, 1–66 (2007).
4. Rees, M. J., Begelman, M. C., Blandford, R. D. & Phinney, E. S. Ion-supported tori and the origin of radio jets. *Nature* **295**, 17–21 (1982).
5. Narayan, R., McClintock, J. E. & Yi, I. A new model for black hole soft X-ray transients in quiescence. *Astrophys. J.* **457**, 821 (1996).
6. Shakura, N. I. & Sunyaev, R. A. Black holes in binary systems. Observational appearance. *Astron. Astrophys.* **24**, 337–355 (1973).
7. Steiner, J. F. et al. The constant inner-disk radius of LMC X-3: a basis for measuring black hole spin. *Astrophys. J.* **718**, L117–L121 (2010).
8. Plant, D. S., Fender, R. P., Ponti, G., Muñoz-Darias, T. & Coriat, M. Revealing accretion on to black holes: X-ray reflection throughout three outbursts of GX 339–4. *Mon. Not. R. Astron. Soc.* **442**, 1767–1785 (2014).
9. Ingram, A. & Done, C. A physical model for the continuum variability and quasi-periodic oscillation in accreting black holes. *Mon. Not. R. Astron. Soc.* **415**, 2323–2335 (2011).
10. Fabian, A. C. et al. On the determination of the spin and disc truncation of accreting black holes using X-ray reflection. *Mon. Not. R. Astron. Soc.* **439**, 2307–2313 (2014).
11. García, J. A. et al. X-ray reflection spectroscopy of the black hole GX 339–4: exploring the hard state with unprecedented sensitivity. *Astrophys. J.* **813**, 84 (2015).
12. Fabian, A. C. et al. Broad line emission from iron K- and L-shell transitions in the active galaxy 1H0707-495. *Nature* **459**, 540–542 (2009).
13. Uttley, P., Cackett, E. M., Fabian, A. C., Kara, E. & Wilkins, D. R. X-ray reverberation around accreting black holes. *Astron. Astrophys. Rev.* **22**, 72 (2014).
14. Zoghbi, A., Fabian, A. C., Reynolds, C. S. & Cackett, E. M. Relativistic iron K X-ray reverberation in NGC 4151. *Mon. Not. R. Astron. Soc.* **422**, 129–134 (2012).
15. Kara, E. et al. A global look at X-ray time lags in Seyfert galaxies. *Mon. Not. R. Astron. Soc.* **462**, 511–531 (2016).
16. Uttley, P. et al. The causal connection between disc and power-law variability in hard state black hole X-ray binaries. *Mon. Not. R. Astron. Soc.* **414**, L60–L64 (2011).
17. De Marco, B., Ponti, G., Muñoz-Darias, T. & Nandra, K. Tracing the reverberation lag in the hard state of black hole X-ray binaries. *Astrophys. J.* **814**, 50 (2015).
18. De Marco, B. et al. Evolution of the reverberation lag in GX 339–4 at the end of an outburst. *Mon. Not. R. Astron. Soc.* **471**, 1475–1487 (2017).
19. Kawamuro, T. et al. MAXI/GSC detection of a probable new X-ray transient MAXI J1820+070. *Astron. Telegr.* 11399 (2018).
20. Uttley, P. et al. NICER observations of MAXI J1820+070 suggest a rapidly-brightening black hole X-ray binary in the hard state. *Astron. Telegr.* 11423 (2018).
21. Tucker, M. A. et al. ASASSN-18ey: the rise of a new black-hole X-ray binary. *Astrophys. J.* **867**, L9 (2018).

22. Gendreau, K. C. et al. The Neutron star Interior Composition Explorer (NICER): design and development. *Proc. SPIE* **9905**, 99051H (2016).
23. Díaz Trigo, M., Sidoli, L., Boirin, L. & Parmar, A. N. XMM-Newton observations of GX 13 + 1: correlation between photoionised absorption and broad line emission. *Astron. Astrophys.* **543**, A50 (2012).
24. Homan, J. et al. NICER observations of MAXI J1820+070: continuing evolution of X-ray variability properties. *Astron. Telegr.* 11576 (2018).
25. Gandhi, P., Rao, A., Johnson, M. A. C., Paice, J. A. & Maccarone, T. J. Gaia DR2 distances and peculiar velocities for Galactic black hole transients. Preprint at https://arxiv.org/abs/1804.11349 (2018).
26. Miyamoto, S. & Kitamoto, S. X-ray time variations from Cygnus X-1 and implications for the accretion process. *Nature* **342**, 773 (1989).
27. Altamirano, D. & Méndez, M. The evolution of the X-ray phase lags during the outbursts of the black hole candidate GX 339–4. Mon. *Not. R. Astron. Soc.* **449**, 4027–4037 (2015).
28. Papadakis, I. E., Nandra, K. & Kazanas, D. Frequency-dependent time lags in the X-ray emission of the Seyfert galaxy NGC 7469. *Astrophys. J.* **554**, L133–L137 (2001).
29. Kotov, O., Churazov, E. & Gilfanov, M. On the X-ray time-lags in the black hole candidates. *Mon. Not. R. Astron. Soc.* **327**, 799–807 (2001).
30. Parker, M. L. et al. NuSTAR and Suzaku observations of the hard state in Cygnus X-1: locating the inner accretion disk. *Astrophys. J.* **808**, 9 (2015).

Acknowledgements E.K. thanks G. Ryan and P. Teuben for discussions on ways to speed up the Python code and J. Garcia and D. Buisson for discussions on NuSTAR observations of MAXI J1820+070. E.K. acknowledges support from the Hubble Fellowship Program and the University of Maryland Joint Space Science Institute and the Neil Gehrels Endowment in Astrophysics through the Neil Gehrels Prize Postdoctoral Fellowship. Support for program number HST-HF2-51360.001-A was provided by NASA through a Hubble Fellowship grant from the Space Telescope Science Institute, which is operated by the Association of Universities for Research in Astronomy, Inc., under NASA contract NAS5-26555. J.F.S. was supported by NASA Einstein Fellowship grant PF5-160144. E.M.C. acknowledges NSF CAREER award AST-1351222. D.A. acknowledges support from the Royal Society. This work was supported by NASA through the NICER mission and the Astrophysics Explorers Program, and made use of data and software provided by the High Energy Astrophysics Science Archive Research Center (HEASARC).

Reviewer information *Nature* thanks D. Haggard and the other anonymous reviewer for their contribution to the peer review of this work.

Author contributions E.K. led timing analysis and interpretation of results. J.F.S. produced the HID and contributed to interpretation of results. A.C.F. performed spectral modelling and contributed to interpretation of results. E.M.C. and P.U. performed cross-checks of analysis software and contributed to interpretation of results. R.A.R. contributed to background modelling and interpretation of results. K.C.G. and Z.A. scheduled the NICER observations and contributed to data reduction. D.A., J.H., S.E., T.E., J.N. and A.L.S. contributed to interpretation of results.

Competing interests The authors declare no competing interests.

Additional information
Extended data is available for this paper at https://doi.org/10.1038/s41586-018-0803-x.
Reprints and permissions information is available at http://www.nature.com/reprints.
Correspondence and requests for materials should be addressed to E.K.
Publisher's note: Springer Nature remains neutral with regard to jurisdictional claims in published maps and institutional affiliations.

METHODS

Data reduction. The data were processed using NICER data-analysis software (DAS version 2018-03-01 V003). The data were cleaned using standard calibration with NICERCAL and screening with NIMAKETIME. To filter out high-background regions, we made a cut on the magnetic cut-off rigidity with COR SAX > 4. We selected events that were not flagged as 'overshoots' or 'undershoots' (EVENT FLAGS = bxxxx00) and events that were detected outside the South Atlantic Anomaly. We also omitted forced triggers. We required pointing directions at least 30° above the Earth limb and 40° above the bright Earth limb. The cleaned events, produced with NICERMERGECLEAN, use standard 'trumpet' filtering to eliminate additional known background events. The cleaned events were barycentre-corrected. For the spectra, we estimated in-band background from the 13–15-keV and trumpet-rejected count rates, and used this to select the appropriate background model from observations of a blank field. To reduce the strong localized residuals that result from calibration uncertainties, the spectra of MAXI J1820+070 were corrected using residuals from fits to the featureless power-law spectra of the Crab nebula[31]. This accounts for most of the calibration uncertainties, though NICER calibration work is ongoing. We emphasize that small uncertainties in the instrument response do not affect the time lag analysis, because the time lags are a ratio of the imaginary and real parts of the cross-spectrum, and thus, the instrument response is divided out[32]. For the timing analysis, we binned the cleaned events in time and energy to produce uninterrupted light-curve segments of 10 s duration and 0.001 s time bins in multiple energy bands.

Lags in the remaining observations. NICER continues to monitor MAXI J1820+070 with an almost-daily cadence, and so detailed follow-up papers will study the lags of the entire state transition from outburst back to quiescence, but here, we briefly discuss the results from the remaining observations taken thus far.

Beyond our six epochs of interest, we analysed all of the other observations taken between our first and last epoch (that is, from MJD 58,198 to MJD 58,250). We produced lag–frequency spectra between 0.5–1 keV and 1–10 keV (similar to the analysis shown for the six epochs in Fig. 2), and found clear evidence for high-frequency soft lags in all observations. Extended Data Fig. 4a shows the frequency range where soft lags are found. The overall trend is towards higher frequencies over time.

All high-frequency lag–energy spectra of observations between epochs 1 and 6 show clear thermal lags, though Fe K lags are not found in all cases. In the observations where there are no indications of an Fe K lag, it is either because of low signal-to-noise ratio or because it appears that the hard lag continues on to the highest energies. The consistent detection of a thermal reverberation lag (where the signal-to-noise ratio is highest) suggests that the lack of Fe K reverberation in some observations is due not to a change in the reflection, but rather due to something in the continuum (or simply due to low signal-to-noise ratio). This is consistent with our overall interpretation that the corona is driving the evolution of the source.

We analysed the earliest observations taken as the source was rising to peak (observation identification (ObsID) numbers ending 01 to 05, from MJD 58,189 to MJD 58,193; see the dark-red hashed region in the hardness–intensity diagram in Extended Data Fig. 4b). The 0.5–1-keV versus 1–10-keV lag–frequency spectrum shows no statistically significant high-frequency soft lag (see Extended Data Fig. 4c for comparison to the lags in epoch 1 near the peak luminosity). However, examining the lag–energy spectrum in the same frequency range as epoch 1 reveals a soft thermal lag and a dominating continuum hard lag (Extended Data Fig. 4d). Despite showing a clear Fe K emission line (see inset of Extended Data Fig. 4c), there is no evidence for Fe K reverberation, perhaps because it is 'hidden' in the strong continuum hard lag. This result is perhaps consistent with our proposed picture in which the corona is highly extended at early times, and thus dominates the lags, even up to high frequencies.

High-frequency soft lags above 10 Hz remain throughout all of the hard-state observations, even as the luminosity drops by a factor of four. Then, at MJD 58,290, MAXI J1820+070 began a rapid transition to the soft state. It is well known in many Galactic black-hole transients that the root-mean-square variability greatly decreases as the source transitions to the soft state. We were able to measure high-frequency power above the Poisson noise limit up to MJD 58,304.9 (by which time the spectral hardness has decreased from 0.29 to 0.17). Even as the source began to transition from the hard to the soft state, we continued to observe soft lags at very high frequencies (see Extended Data Fig. 4e for a comparison of the lag–frequency spectrum from ObsIDs 94 to 96 taken from MJD 58,302 to MJD 58,304.9 and the lag–frequency spectrum of epoch 6 in the hard state). As the source transitioned to the soft state and the root-mean-square variability decreased, the quality of the lag–energy spectra decreased, but they are consistent with the hard state lag–energy spectra (see Extended Data Fig. 4f).

Significance tests in the lag–frequency spectra. See Fig. 2. To measure the significance of the reversal of the sign in the lag–frequency spectra shown in Fig. 2, we fitted the 1–100 Hz lag–frequency spectra of all six epochs in XSPEC. We compared two simple models: a null hypothesis with a power-law lag that decays to zero lag at high frequencies, and a model with a power-law lag plus an additional negative Gaussian to fit the high-frequency soft lag. Comparing the change in χ^2 per degree of freedom (d.o.f.), we found that the model with the additional negative Gaussian was preferred in all epochs at 4.5σ confidence or greater.

The frequency at which the lag switches from positive to negative increases by roughly an order of magnitude over the six epochs. From the binned lag–frequency spectra in Fig. 2, the turnover frequencies for our six epochs of interest are: 2.8 Hz, 5.6 Hz, 7.9 Hz, 11.1 Hz, 15.7 Hz and 22.0 Hz. The frequency ranges from all epochs do overlap, though we strongly disfavour a solution where the frequency range of the soft lag is constant over time. We tested this by fitting all six lag–frequency spectra simultaneously with the power law plus negative Gaussian model. Our null hypothesis is that the mean frequency, width and amplitude of the Gaussian is constant over all epochs, and compare this to a model where the Gaussian parameters are allowed to vary. The variable Gaussian model results in an improved fit of $\Delta\chi^2 = 150$ for 15 fewer degrees of freedom. Thus, the soft lag is increasing in frequency at more than 8σ confidence.

Significance tests and amplitudes in the lag–energy spectra. See Fig. 3. NICER allows us to probe higher-frequency time lags better than ever before, revealing the evolution of the thermal lag to higher frequencies and potential structure at the Fe K band. Despite this advance, we cannot be sure that we are probing frequencies beyond which the hard continuum lag no longer contributes to the lag–energy spectrum. This complicates the measurements of the significance and amplitude of the Fe K lag. In this and the following section, we examined two cases: first, assuming that the hard continuum lag is not contributing to the lags (that is, assuming that the power-law continuum responds simultaneously over all bands, referred to as case A); and second, assuming that the hard lag is still present (referred to as case B).

We fitted the 0.5–10-keV lag–energy spectrum (Fig. 3) of all six epochs in XSPEC. We fitted the lag–energy spectrum with a null continuum model and compared it to the continuum plus lines model. In our case, the null-continuum model is a power-law hard lag and a thermal lag (in XSPEC syntax: MODEL POWERLAW+DISKBB). In case A, the temperature and normalizations are left free to vary, and the power-law index is fixed at zero. In case B, the power-law index is also left free to vary, similar to the null hypothesis in ref. [18]. We then compared these to the null continuum plus a broad Fe K component and a broad Fe L component. We used the relativistically broadened Fe line as prescribed in the LAOR model. For simplicity, we fixed the inclination to 45°, the emissivity profile to r^{-3}, the inner-disk radius to the minimum value $1.235r_g$, and the outer-disk radius to $1{,}000r_g$. The normalization and line energy are the only free parameters of the model. The final significance of the results is not sensitive to the parameters of the LAOR model, changing by <10% when the inclination is left free to vary.

Extended Data Fig. 3 demonstrates the results of lag fitting for the first observation (ObsID 1200120106) for cases A and B. Details on the fitting parameters for all six epochs can be found in Extended Data Table 2 and Extended Data Table 3. Comparing the change in χ^2 per degree of freedom, we found that the addition of the Fe lags in case A is significant (3.5σ or greater). In all cases, however, distinguishing between a pure power-law hard lag and a hard lag with an Fe L and Fe K lag is less easy, and the significance ranges from 1σ to 6.5σ. The significance of the Fe L line alone is stronger than Fe K alone, as the signal-to-noise ratio at 1 keV is much higher than in the Fe K band. These quoted significances are for the individual epochs of interest and do not account for the total number of trials from all NICER observations of MAXI J1820+070 (as the observations were not selected for the presence of the Fe line). Although we did observe peaks in the lag–energy spectra at the energies where we expect Fe L and Fe K reverberation, not all features detected here are formally statistically significant.

Assuming that the lag features at about 7 keV are associated with Fe K reverberation lags, we measured the lag amplitude as the difference between the peak of the Fe K lag and the power-law normalization in that band. The case A continuum always results in the largest lag amplitude, because any hard lag contribution decreases the inferred amplitude of the lag. In the main text, we quote the case A lag amplitude as a conservative measure of the Fe K lag. For completeness and for comparison to previous results[17,18], we also measured the amplitude of the thermal lag as the difference between the power-law normalization and the maximum lag below 1 keV. The thermal lags in MAXI J1820+070 are both smaller in amplitude and appear at higher frequencies than in previous observations of black-hole binaries with XMM-Newton[16–18]. See Extended Data Tables 2 and 3 for the inferred thermal lag and Fe K lag using these methods. The average Fe K lag amplitude using the case A continuum model is 0.47 ± 0.08 ms or $(14 \pm 3)r_g/c$ for a $10M_\odot$ black hole.

Converting the lag into a light travel distance. Fe K lags are not a direct measure of the light travel time between the corona and the accretion disk. Effects such as the geometry of the system, inclination to the observer and relativistic Shapiro delay all play a part in the interpretation of the measured lags as physical distances. In this section, we discuss the two major contributors that are not directly

related to light-travel time, but have competing effects on the interpretation of the observed lag amplitude as a light travel distance. These contributors are the effect of dilution (that is, the fact that the lag is measured between energy bands, all of which contain varying contributions from broadband spectral components), and the effect of propagating fluctuations that contribute to the lags on a range of timescales.

Dilution is caused by the presence of emission from both the driving continuum and reflection in each bin of interest. Its main effect is to reduce the measured amplitude of the lags by a factor of $R/(1+R)$, where R is the relative amplitude of the variable, reflected flux to the variable, continuum flux in the bin of interest. In AGN systems, the dilution factor increases the inferred light travel time by a factor of a few[13], though in stellar-mass black holes, where the disk is typically more highly ionized and reflection fractions are lower, the effect could be much higher. Dilution should be treated as part of a full frequency-dependent spectral-timing model, which is beyond the scope of this work.

Propagating fluctuations in the disk modulate the hard X-ray emission produced through inverse Compton upscattering of thermal disk photons. These propagation lags could contribute up to the highest frequencies (for example, up to the orbital frequency at the innermost stable circular orbit), and could be contributing to the interpretation of the reverberation lag at high frequencies. This effect is being explored further (ref. [33] and P. U. & J. Malzac, manuscript in preparation). The effect of including propagation lags in the high-frequency lag–energy spectrum is that the inferred light travel distance from the corona to the disk decreases by a factor of a few.

For now, we have demonstrated these effects on the time lags from the first epoch using the same technique as in previous studies of the soft thermal lags[18]. We fitted the lag–energy spectra with the same power-law, blackbody, 2 LAOR model (as in the previous section), allowing for a non-zero power-law index for the continuum lag component (that is, allowing some contribution from the continuum lag; case B). We measured the time delay between the continuum model and the measured lags within 6–7 keV to be 0.36 ± 0.13 ms. We then estimated the effects of dilution based on the results of spectral fitting to the time-integrated energy spectrum (A.C.F. et al., manuscript in preparation). The dilution factor is taken to be the ratio of the reflection component flux to the power-law flux in the 6–7-keV band (that is, the band over which we measured the time lag). We found $R_{6\text{–}7\,\mathrm{keV}} = 0.44$, which means that the intrinsic lags are reduced by a factor of $R_{6\text{–}7\,\mathrm{keV}}/(1+R_{6\text{–}7\,\mathrm{keV}}) = 0.3$. This suggests that the intrinsic lags are about 1 ms or about $30(r_g/c)$ for a $10M_\odot$ black hole, although there are known caveats. Measuring the Fe K lag with respect to a continuum model implicitly assumes that there is no reflection in the reference band (an unlikely scenario), and thus the dilution factor described above and in previous works are likely lower bounds.

Lags in other wavebands. X-ray time lags in both AGN and stellar-mass black holes provide information on the accretion flow at the smallest scales, closest to the black hole. Multi-wavelength time lags between X-ray, ultraviolet and optical regions of the spectrum have revealed much longer time lags that allow us to probe the accretion flow at larger scales in both AGN[34,35] and in Galactic black-hole transients[36,37]. In Galactic black-hole binaries, multiwavelength time lag analysis probes emitting regions at thousands of gravitational radii (either from reprocessing off the outer optically emitting disk or from the infrared/optical emitting part of the jet. Joint NICER and optical monitoring campaigns of MAXI J1828+070 are ongoing, and will be presented in future papers (A. Townsend et al., manuscript in preparation, and P.U. et al., manuscript in preparation).

Code availability. The model fitting of spectra and lag–energy spectra was completed with XSPEC, which is available at the HEASARC website (https://heasarc.gsfc.nasa.gov/). The timing analysis was performed with Python code that is at present not publicly available; however, community efforts (by members of our team and others) are currently being made to aggregate Python timing analysis codes into one open-source package called Stingray (see https://github.com/StingraySoftware/stingray). All figures were made in Veusz, the Python-based scientific plotting package, developed by J. Sanders and available at https://veusz.github.io/.

Data availability

The datasets analysed during this study are available at NASA's High Energy Astrophysics Science Archive Research Center (HEASARC; https://heasarc.gsfc.nasa.gov/).

31. Ludlam, R. M. et al. Detection of reflection features in the neutron star low-mass X-ray binary Serpens X-1 with NICER. *Astrophys. J.* **858**, L5 (2018).
32. Mastroserio, G., Ingram, A. & van der Klis, M. Multi-time-scale X-ray reverberation mapping of accreting black holes. *Mon. Not. R. Astron. Soc.* **475**, 4027–4042 (2018).
33. Mahmoud, R. D., Done, C. & De Marco, B. Reverberation reveals the truncated disc in the hard state of GX 339-4. Preprint at https://arxiv.org/abs/1811.06911 (2018).
34. Fausnaugh, M. M. et al. Space telescope and optical reverberation mapping project. III. Optical continuum emission and broadband time delays in NGC 5548. *Astrophys. J.* **821**, 56 (2016).
35. Edelson, R. et al. Swift monitoring of NGC 4151: evidence for a second X-ray/UV reprocessing. *Astrophys. J.* **840**, 41 (2017).
36. Gandhi, P. et al. Furiously fast and red: sub-second optical flaring in V404 Cyg during the 2015 outburst peak. *Mon. Not. R. Astron. Soc.* **459**, 554–572 (2016).
37. Vincentelli, F. M. et al. Characterization of the infrared/X-ray subsecond variability for the black hole transient GX 339-4. *Mon. Not. R. Astron. Soc.* **477**, 4524–4533 (2018).

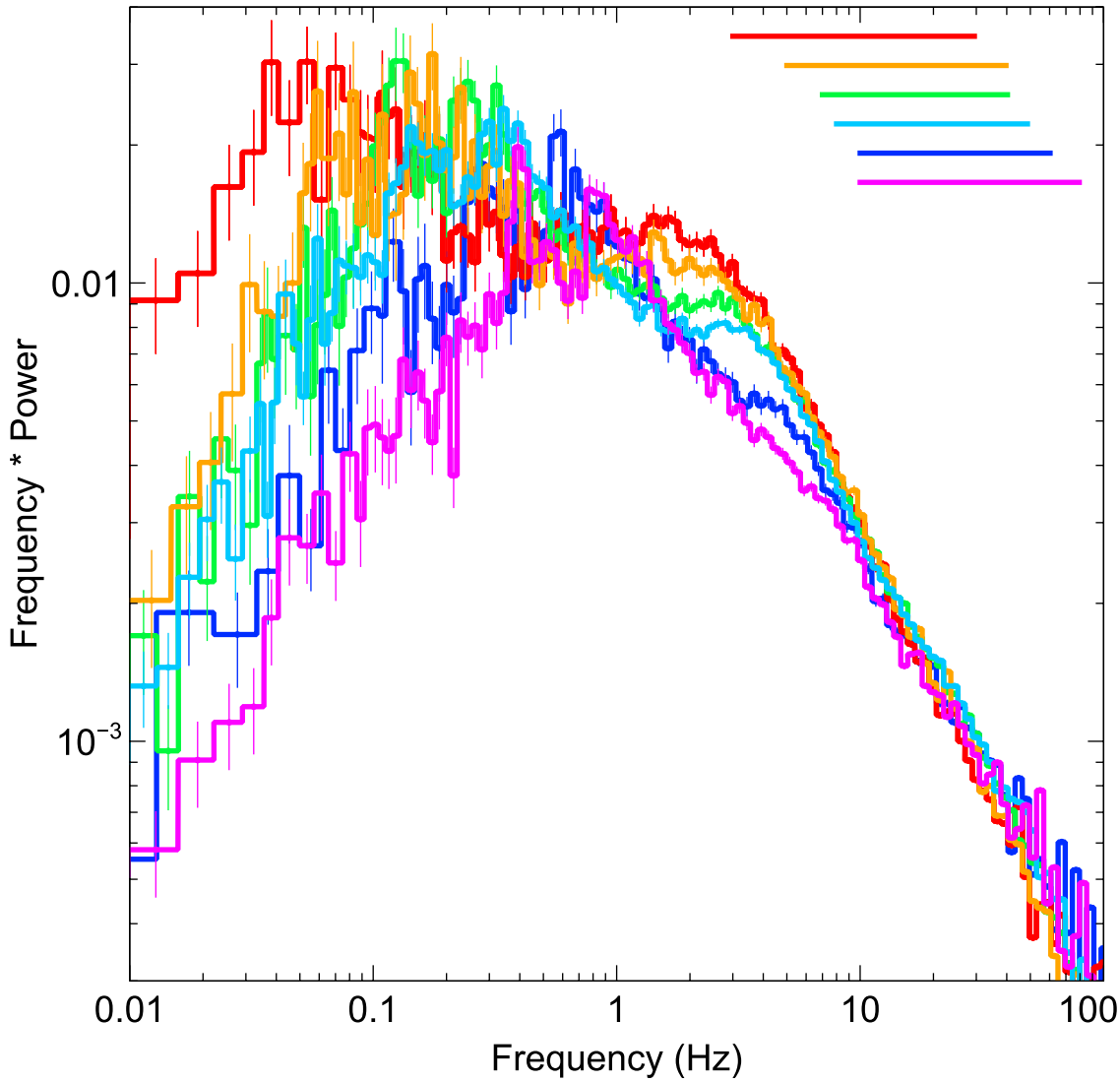

Extended Data Fig. 1 | The power spectral evolution. The 0.3–10-keV Poisson noise-subtracted power spectra (in units of (root-mean-square/mean)^2 with 1σ errors) for the six epochs of interest (same colour scheme throughout). The solid lines on the top-right portion of the figure indicate the frequencies used in the lag–energy analysis (Fig. 3).

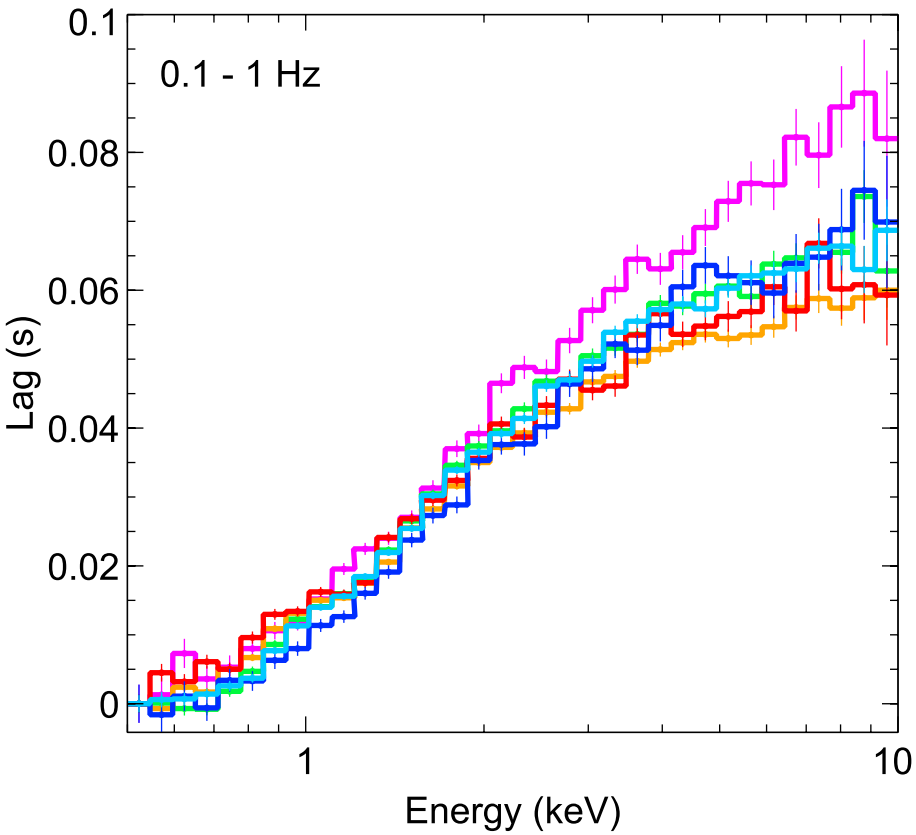

Extended Data Fig. 2 | The low-frequency lag–energy spectra. The low-frequency (0.1–1-Hz) lag–energy spectra for the six epochs. The lags have been shifted such that the lowest-energy lag starts at zero. No thermal lag is seen at low frequencies. Error bars indicate 1σ confidence intervals.

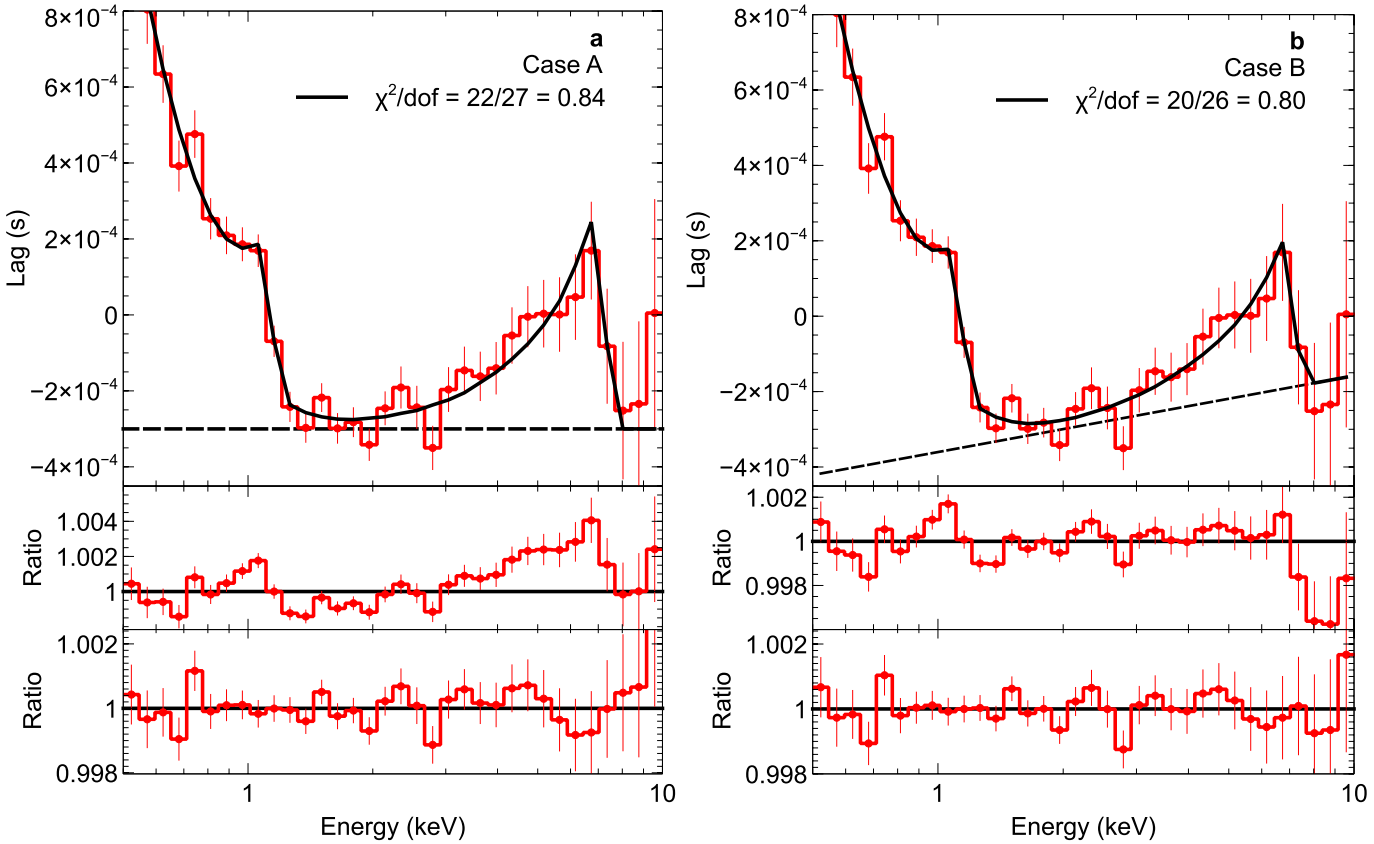

Extended Data Fig. 3 | Modelling the lag–energy spectra. a, Case A; **b**, case B. The top panels show the best-fitting models fitted to epoch 1 (ObsID 1200120106), demonstrating how the significance and amplitude of the Fe K lag are determined. The middle panels show the ratio of the data to the null hypothesis (POWERLAW+DISKBB). The case A null hypothesis is assuming a continuum lag power-law index of zero, whereas case B allows for a non-zero continuum lag. The bottom panels show the ratio of the data to the best-fitting model (POWERLAW+DISKBB+LAOR+LAOR), again where case B allows for a non-zero power-law continuum lag. See text and Extended Data Table 2 for details on the best-fit parameters and χ^2 fit statistics. Error bars indicate 1σ confidence intervals.

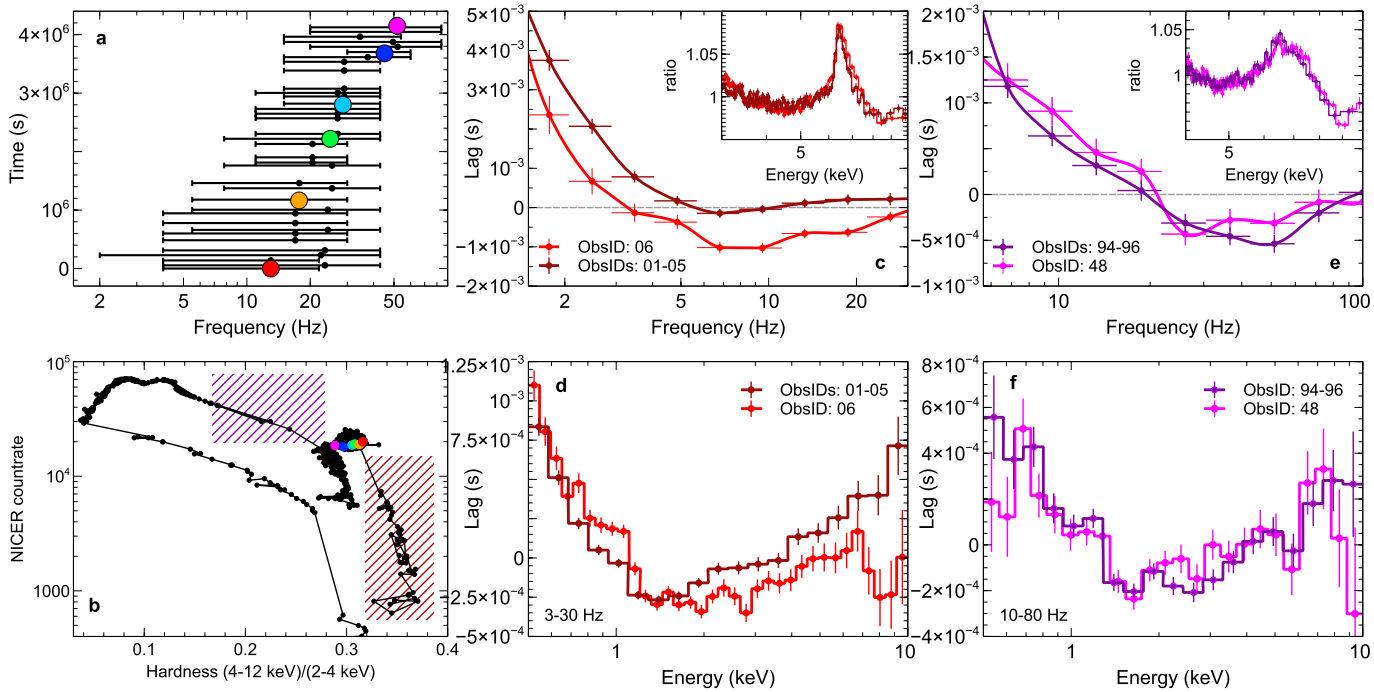

Extended Data Figure 4 | Lags from other observations. a, The frequency range of the high-frequency soft lags (lags between 0.5–1 keV and between 1–10 keV) for all observations between epoch 1 and 6. The general trend is that the soft lags increase to higher frequencies over time. The coloured dots show the frequency ranges for the six epochs studied. **b**, The hardness–intensity diagram, defined as the total 0.2–12-keV count rate versus the ratio of hard (4–12 keV) to soft (2–4 keV) count rates (as in Fig. 1c) for all available data up to MJD 58,344. This extended hardness–intensity diagram shows the recent transition to the soft state. In the right two panels, we show the lags from the earliest observations from the beginning of the outburst (dark-red hashed region) and from the latest times where we can measure high-frequency time lags, at the beginning of the transition to the soft state (purple hashed region). **c**, Comparison of the lag–frequency spectrum of the first epoch (ObsID 06) and the five co-added ObsIDs that preceded it (MJD 58,189 to MJD 58,193). The inset shows a comparison of the ratio of the energy spectra in these epochs to a power-law fit in the range 3–10 keV. **d**, The corresponding lag–energy spectra for the 3–30-Hz range, where Fe K lags were seen in epoch 1. The earlier observations (ObsIDs 01–05) show a dominating hard lag at high energies, and no evidence for Fe K lags. **e**, **f**, As in **c** and **d**, but comparing the lag–frequency spectra and lag–energy spectra of epoch 6 to later observations as the source begins to transition to the soft state. Error bars indicate 1σ confidence intervals.

Extended Data Table 1 | Overview of the observations used in this analysis

Epoch	Date	ObsID	Exposure (s)	0.2-12 keV Count rate (cts/s)
1	2018-03-21	1200120106	5438	20568
2	2018-04-04	1200120120	6487	19015
3	2018-04-16	1200120130	10619	18931
4	2018-04-21	1200120134	6964	18487
	2018-04-23	1200120135	3692	18731
5	2018-05-02	1200120142	5512	17983
6	2018-05-08	1200120148	4260	18403

The count rate is for 52 active detectors.

Extended Data Table 2 | Fit parameters of the case A model

Case A						
Epoch	1	2	3	4	5	6
A_{po} ($\times 10^{-4}$ s)	-3.0 ± 0.3	-2.7 ± 0.3	-2.4 ± 0.2	-2.1 ± 0.3	-2.0 ± 0.6	-1.5 ± 0.4
T_{diskbb} (eV)	20 ± 4	20 ± 4	21^{+4}_{-6}	22 ± 5	19 ± 5	23^{+14}_{-8}
E_{laor1} (keV)	$6.5^{+0.2}_{-0.4}$	$7.3^{+0.4}_{-0.6}$	$6.8^{+1}_{-0.4}$	$6.7^{+0.5}_{-0.3}$	$7.8^{+0.9}_{-0.6}$	$7.2^{+0.5}_{-0.7}$
E_{laor2} (keV)	1.02 ± 0.02	$0.98^{+0.02}_{-0.04}$	$0.85^{+0.50}_{-0.09}$	$1.01^{+0.07}_{-0.04}$	$0.77^{+0.13}_{-0.08}$	$1.18^{+0.08}_{-0.06}$
$\Delta\chi^2$/d.o.f.	105/4	69/4	20/4	53/4	19/4	27/4
Fe K lag amplitude ($\times 10^{-4}$ s)	4.7 ± 1.3	4.5 ± 1.3	4.0 ± 2.4	3.6 ± 0.9	6.6 ± 2.9	4.8 ± 1.8
Thermal lag amplitude ($\times 10^{-4}$ s)	14.0 ± 1.0	14.0 ± 1.1	17.1 ± 1.6	10.5 ± 1.3	10.7 ± 2.9	6.5 ± 1.4

Results of the lag fitting to measure the Fe K lag amplitude and thermal lag amplitude. A_{po} is the lag amplitude of the continuum component, modelled as a power law with index fixed at zero (case A). T_{diskbb} is the temperature of the inner disk for a multi-colour disk blackbody component. E_{laor1} and E_{laor2} are the energies of the LAOR components. The Fe K lag and thermal lag amplitude are the difference between the peak of the Fe K and thermal lag components and A_{po}. Error bars represent 90% confidence intervals.

Extended Data Table 3 | Fit parameters of the case B model

Case B						
Epoch	1	2	3	4	5	6
$A_{\rm po}$ ($\times 10^{-4}$ s)	$-3.6^{+0.7}_{-1.0}$	-3.7 ± 1	-3.3 ± 0.2	-3.1 ± 0.9	$-2.6^{+1.4}_{-2.2}$	-2.5 ± 1.0
$\Gamma_{\rm po}$ ($\times 10^{-3}$)	0.89 ± 0.11	$1.3^{+1.2}_{-1.3}$	0.5 ± 1.5	$1.3^{+1.0}_{-1.2}$	$1.2^{+1.9}_{-2.2}$	1.3 ± 1.5
$T_{\rm diskbb}$ (eV)	23^{+7}_{-5}	25^{+7}_{-6}	22^{+7}_{-9}	26^{+8}_{-6}	24 ± 12	28^{+18}_{-11}
$E_{\rm laor1}$ (keV)	$6.4^{+0.3}_{-0.4}$	$7.2^{+0.8}_{-1.2}$	$6.8^{+1.1}_{-0.6}$	$6.8^{+0.7}_{-0.8}$	$7.9^{+0.07}_{-1.9}$	$7.1^{+0.9}_{-1.0}$
$E_{\rm laor2}$ (keV)	1.02 ± 0.02	$0.98^{+0.02}_{-0.04}$	$0.84^{+3.0}_{-2.3}$	$1.02^{+0.08}_{-0.05}$	$0.76^{+9.0}_{-0.2}$	$1.18^{+0.08}_{-0.06}$
$\Delta\chi^2$/d.o.f.	44/4	19/4	4/4	10/4	4/4	12/4
Fe K lag amplitude ($\times 10^{-4}$ s)	3.6 ± 1.3	2.8 ± 1.3	3.5 ± 1.3	2.1 ± 0.9	3.2 ± 2.5	3.1 ± 1.8
Thermal lag amplitude ($\times 10^{-4}$ s)	15.2 ± 0.9	15.9 ± 1.0	17.7 ± 1.6	12.2 ± 1.2	12.1 ± 2.9	8.1 ± 1.3

As for Extended Data Table 2, but for the null-continuum-model case B, where the power-law index $\Gamma_{\rm po}$ is free to vary.